View Article Online
View Journal

Green Chemistry

Cutting-edge research for a greener sustainable future

Accepted Manuscript

This article can be cited before page numbers have been issued, to do this please use: X. Gao, C. Li, J. Liu, S. Xu, K. Chen and G. Zhao, *Green Chem.*, 2026, DOI: 10.1039/D6GC01435F.

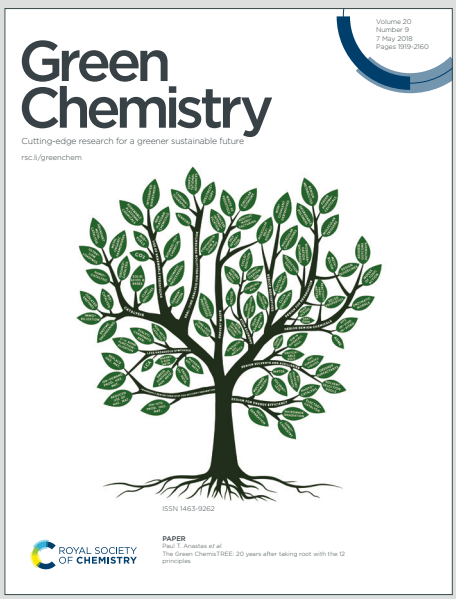

ROYAL SOCIETY OF CHEMISTRY

rsc.li/greenchem

View Article Online
DOI: 10.1039/D6GC01435F

Green foundation box

1. A novel, mild, one-step electrocatalytic route converting waste CO_2 and benzylamine into N-benzylformamide is proposed.
2. We achieve a Faradaic efficiency of 33.4% and a yield of 53 $mmol \cdot L^{-1} \cdot h^{-1}$ for the electrocatalytic synthesis of N-benzylformamide at –3.8 V over C-O-SnPc catalyst for the first time and confirmed a *COOH-mediated C-N coupling pathway through *in situ* measurements and theoretical calculations.
3. The greenness of this work could be further enhanced by coupling the electrocatalytic process with renewable electricity sources such as solar or wind power, minimizing the carbon footprint of the energy input. Additionally, expanding the substrate scope to include real waste streams containing dilute amines would improve environmental relevance and resource circularity.

View Article Online
DOI: 10.1039/D6GC01435F

ARTICLE

Achieving selective synthesis of N-benzylformamide via one-step electrocatalytic C-N coupling of CO_2 and benzylamine

Received 00th January 20xx,
Accepted 00th January 20xx

DOI: 10.1039/x0xx00000x

Xiaoqian Gao, Chufan Li, Jingyan Liu, Shaohan Xu, Kuang Chen, and Guohua Zhao*

The pressing demands of CO_2 emission reduction and organic amine pollutant treatment motivate the development of electrocatalytic C-N coupling toward resource recovery and green synthesis. The key challenge lies in co-activating both reactants while suppressing CO_2 excessive reduction. Herein, we report the first efficient one-step electrocatalytic synthesis of N-benzylformamide from CO_2 and benzylamine under mild conditions over a bridging-oxygen coordinated tin phthalocyanine catalyst (C-O-SnPc). At –3.8 V, it achieved a current density of 32 mA·cm^{-2}, a Faradaic efficiency of 33.4%, and a yield of 53 mmol·L^{-1}·h^{-1}. *In situ* experiments identified key intermediates *COOH and *PhCH$_2$NHCOOH, confirming a *COOH-mediated pathway. Theoretical calculations revealed oxygen coordination created a multifunctional electron-deficient Sn center. It polarized N-H bond and initiated an electron-withdrawing chain that enhanced *COOH electrophilicity, facilitating the nucleophilic attack (C-N bonding). It also reduced the hydrogenation barrier from *PhCH$_2$NHCOOH to *PhCH$_2$NHCH$_2$O$_2$. This work provides a green strategy for resource recovery and upgrading CO_2 and amines into high-value amides.

Introduction

CO_2 emission reduction and the treatment of organic amine environmental pollutants are pressing environmental challenges.[1-3] Converting CO_2 and organic amines into high-value nitrogen-containing compounds (N-formylation and N-methylation products) via electrochemical C-N coupling reactions represents a dual strategy that enables resource recovery while advancing green chemical synthesis.[4, 5] Notably, the synthesis of formamides (e.g., N-benzylformamide) from CO_2 and amines has been demonstrated in thermocatalysis.[6-8] Cui et al. reported a $CuAlO_x$ thermocatalyst for N-formylation using CO_2 yielding various amines.[9] Specifically, using 1 mmol benzylamine as the substrate, the yield of N-benzylformamide attained 95% over 24 h at 150 °C under 3 MPa H_2 and 1 MPa CO_2. However, it typically requires high temperature and pressure, and often involves hydrogenation reagents or complex catalyst systems.[10] Compared to such energy-intensive thermal processes, electrocatalytic C-N coupling offers a more sustainable pathway. Furthermore, C-N coupling expands the range of high-value carbon utilization products, compared to CO_2 reduction reaction (CO_2RR), with nitrogen-containing compounds finding extensive applications in pharmaceuticals, biotechnology, and materials science.[11]

Recent research has intensively focused on C-N coupling between CO_2 and inorganic nitrogen sources, achieving efficient synthesis of products such as urea and formamides.[12-15] The reduction of inorganic nitrogen sources typically involves multi-electron transfer,[16, 17] whereas organic amines as nitrogen sources require only activation of the N-H bond on -NH_2 to participate in reactions. Therefore, exploring novel reaction pathways and electrocatalytic systems to achieve CO_2 and organic amine C-N coupling holds significant application potential. Herein, we focus on the electrocatalytic C-N coupling of CO_2 with benzylamine for the synthesis of N-benzylformamide (PhCH$_2$NHCHO, a key intermediate in pharmaceutical and fine chemical industries[18]), and efficiently drive this reaction via the precise regulation of active sites.

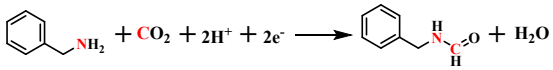

(1)

The one-step electrocatalytic route as depicted in Eq. (1) directly converts CO_2 and benzylamine into the target product N-benzylformamide without any intermediate separation or additional activation processes.

Currently, some progress has been made in the fields of electrolytic C-N coupling of CO_2 with organic amines. Zou et al. reported a Pd/Cu-V_{Cu} catalyst for the electrochemical C-N coupling of CO_2 and dimethylamine to synthesize N, N-dimethylformamide (DMF).[19] Cu vacancies promoted CO_2 adsorption on the catalyst surface, followed by spontaneous coupling with dimethylamine to form C-N bonds. Zhao et al. also reported an InN_3 catalyst for the CO_2 and dimethylamine C-N coupling to synthesize DMF, which promoted the generation of key reaction intermediates *N(CH$_3$)$_2$ and *COOH by modulating its electronic structure.[20] Additionally, Wang et al. reported electrochemical reduction of N-methylation reactions using CO_2, which was achieved with amines, hydroxylamines, and hydrazines as substrates, though the selectivity remained below 10%.[21] During C-N coupling, CO_2 can be activated and reduced into an electrophilic intermediate, which is then nucleophilically attacked by an amine molecule to form a C-N bond. Both the electrophilicity

School of Chemical Science and Engineering, Department of Thoracic Surgery, Shanghai Tongji Hospital, Tongji University, Shanghai 200092, P.R. China.
E-mail: g.zhao@tongji.edu.cn

† Electronic supplementary information (ESI) available.

of the carbon-containing intermediate and the nucleophilicity of the amine molecule significantly influence the coupling performance.[22, 23] Despite these advances, critical challenges remain to be addressed. CO_2 tends to over-reduction into final carbon-containing products rather than participating in coupling, leading to increased byproducts. Besides, the key C-N coupling step exhibits excessively high energy barriers and low selectivity.

Besides, compared with thermocatalytic routes that require high H_2 pressure and elevated temperature, electrocatalytic C-N coupling offers the distinct advantage of operating under ambient conditions without external reducing agents. Moreover, thermal N-formylation often faces the risk of over-reduction to N-methylated byproducts under more forcing reaction conditions (e.g., higher temperature or longer reaction time). In an electrocatalytic system, the reduction depth can in principle be controlled by the applied potential, potentially allowing selective formation of the formamide product while avoiding further hydrogenation. This motivated us to explore whether an electrocatalytic approach could achieve clean N-formylation without N-methylation, a selectivity that is difficult to guarantee in thermal catalysis without meticulous condition control.

Sn-based materials have been proven to be effective catalysts for the electroreduction of CO_2 to produce C1 products (i.e., HCOOH and CO).[24, 25] Specifically, phthalocyanine tin (SnPc) with well-defined structure and single-atom sites supported on hydroxyl-functionalized carbon nanotubes (CNT-OH) have shown promising activity in CO_2RR, mainly due to the adjustment of intermediate adsorption configuration by the oxygen coordination.[26] Notably, we found that the Lewis-acidic Sn sites in SnPc might also interact with the lone-pair electrons of amines,[27, 28] suggesting an underlying dual-function capability of activation of both CO_2 and amines. And electron-deficient sites exhibit superior catalytic activity in promoting the activation and coupling of small molecules.[29] This prompted us to apply SnPc-based catalysts for electrochemical C-N coupling with CO_2 and benzylamine which demands synergistic activation of two reactants. We adopted the bridging oxygen coordination strategy to precisely tailor the electronic structure of Sn center, aiming to enhance its adsorption toward reactants, polarize the N-H bond of benzylamine, and furthermore promote C-N coupling.

Herein, we applied a C-O-SnPc catalyst featuring bridging-oxygen coordination for the electrochemical C-N coupling of CO_2 and benzylamine to synthesize N-benzylformamide. By optimizing the SnPc loading, the catalyst achieved a Faradaic efficiency (FE) of 33.4% and a yield of 53 $mmol \cdot L^{-1} \cdot h^{-1}$ at –3.8 V. Differential charge density indicated that the oxygen coordination rendered the Sn center electron-deficient. This not only polarized the N-H bond of benzylamine to promote deprotonation but also enhanced CO_2 adsorption, stabilized the key *COOH intermediate, and increased its electrophilicity, thereby facilitating nucleophilic attack. *In situ* characterization and theoretical calculations confirmed the *COOH-mediated reaction pathway and demonstrated that bridging oxygen coordination achieved both thermodynamically and kinetically optimization by lowering adsorption energies and reducing the rate-determining step (RDS) barrier.

Experimental section

View Article Online
DOI: 10.1039/D6GC01435F

Chemicals

Phthalocyanine tin (SnPc), ethanol, benzylamine, N-benzylformamide and potassium bicarbonate ($KHCO_3$) were purchased from Adamas Co., Ltd (Shanghai, China). Hydroxyl functionalized multi-walled carbon nanotubes (CNT-OH) and multi-walled carbon nanotubes (CNT) were purchased from Suiheng Technology Co., Ltd. (Shenzhen, China). All chemicals were used without further purification.

Electrocatalytic C-N coupling measurements

C-N coupling experiments were conducted in a membrane electrode assembly (MEA) reactor. 4 mg of the catalyst was dispersed in a mixture solution of 300 μL of ethanol, 150 μL of deionized water and 50 μL of Nafion and then ultrasonicated for 1 h. Catalysts C-O-SnPc-x (x = 1, 2, 3) and SnPc/CNT were synthesized using the method with slight modifications.[26] 40 mg CNT-OH was dispersed in 25 mL ethanol and stirred for 30 min, then different amounts of SnPc (8 mg, 12 mg, 14 mg) were added and the mixtures sonicated for another 30 min. Each resulting suspension was stirred at room temperature for 24 h, and the products were washed with ethanol, then dried in a vacuum oven at 80 °C for 8 h to obtain C-O-SnPc-1, C-O-SnPc-2 and C-O-SnPc-3. SnPc/CNT was synthesized using 40 mg CNT and 12 mg SnPc. Subsequently, the catalyst ink was dropped onto the 2×2 cm carbon paper to form gas diffusion electrode (GDE). The applied potential in electrochemical C-N coupling was tuned by a CHI660e electrochemical workstation. The MEA reactor consisted of two titanium plates featuring a 2×2 cm serpentine flow field. GDE and IrO_x/Ti mesh were used as cathode and anode, respectively. The cathode and anode were separated by a proton exchange membrane (Nafion-117). 0.1 M $KHCO_3$ and CO_2-saturated 0.1 M $KHCO_3$ containing benzylamine were used as anolyte and catholyte, respectively. The flow rate of CO_2 gas was 30 sccm. The detailed electrochemical measurements, product quantitation, *in situ* measurements and catalyst characterization methods are given in ESI.

Computational methods

Density functional theory (DFT) calculations were executed in the Vienna ab initio Simulation Package (VASP)[30-32] with Perdew-Burke-Ernzerhof (PBE) exchange correlation functional and projected augmented wave (PAW) approach. The self-consistent field tolerance accuracy was set at 1×10^{-5} eV per atom and ionic relaxation was set at 0.04 eV/A in all DFT simulation. The SnPc molecular geometry used in calculations is based on the established bent configuration with C_{4v} symmetry and the results of characterization tests, following the model reported by Day et al.[33] Detailed structure optimization was performed after sectioning C-O-SnPc-2 and SnPc/CNT and further loading of metal species for subsequent self-consistent calculations of structure optimization.[34-36] Moreover, the cut-off energy for electronic wave functions was set to 480 eV and k-point grid was set as 2 × 2 × 1 for in-plane hybrid model. ΔG can be expressed as $\Delta G = \Delta E_{DFT} + \Delta ZPE - T\Delta S$, where E_{DFT}, ZPE and S are total energy from DFT calculations, zero-point energy,

View Article Online
DOI: 10.1039/D4GC01658B

and the entropy, respectively. Difference charge density was obtained by following equation: $\Delta\rho = \rho_{AB} - \rho_A - \rho_B$, where ρ_{AB}, ρ_A and ρ_B represent the whole and two subparts, respectively.

Results and discussion

Electrocatalytic C-N coupling

The electrochemical N-formylation of CO_2 and benzylamine was investigated via constant-potential electrolysis. As shown in Fig. 1a and Fig. S1, the reaction was conducted in a membrane electrode assembly (MEA) cell. The catholyte was CO_2-saturated $KHCO_3$ solution containing benzylamine. The zero-gap MEA reactor could effectively improve the mass transfer process of reactions involving gases and enhance the reaction efficiency [37]. The gaseous products H_2, CO were monitored by gas chromatography (Fig. S2), while liquid products formate and N-benzylformamide were detected via NMR spectroscopy. The working electrode was a GDE coated with catalyst, in which different amounts of SnPc was loaded on CNT-OH via π-π stacking interactions (C-O-SnPc-x, x = 1, 2, 3). For comparison, SnPc/CNT was synthesized with SnPc loaded on CNT. Transmission electron microscopy (TEM) and high-angle annular dark-field scanning transmission electron microscopy (HAADF-STEM) images confirmed the tube structure and revealed the presence of Sn single atoms on C-O-SnPc-x and SnPc/CNT (Fig. S3–S6). Moreover, energy dispersive X-ray spectroscopy (EDS) mappings showed uniform distribution of Sn, N, O, and C species on C-O-SnPc-x, while Sn, N, and C species were uniformly distributed on SnPc/CNT, visually demonstrating the successful loading of SnPc. Fourier transform

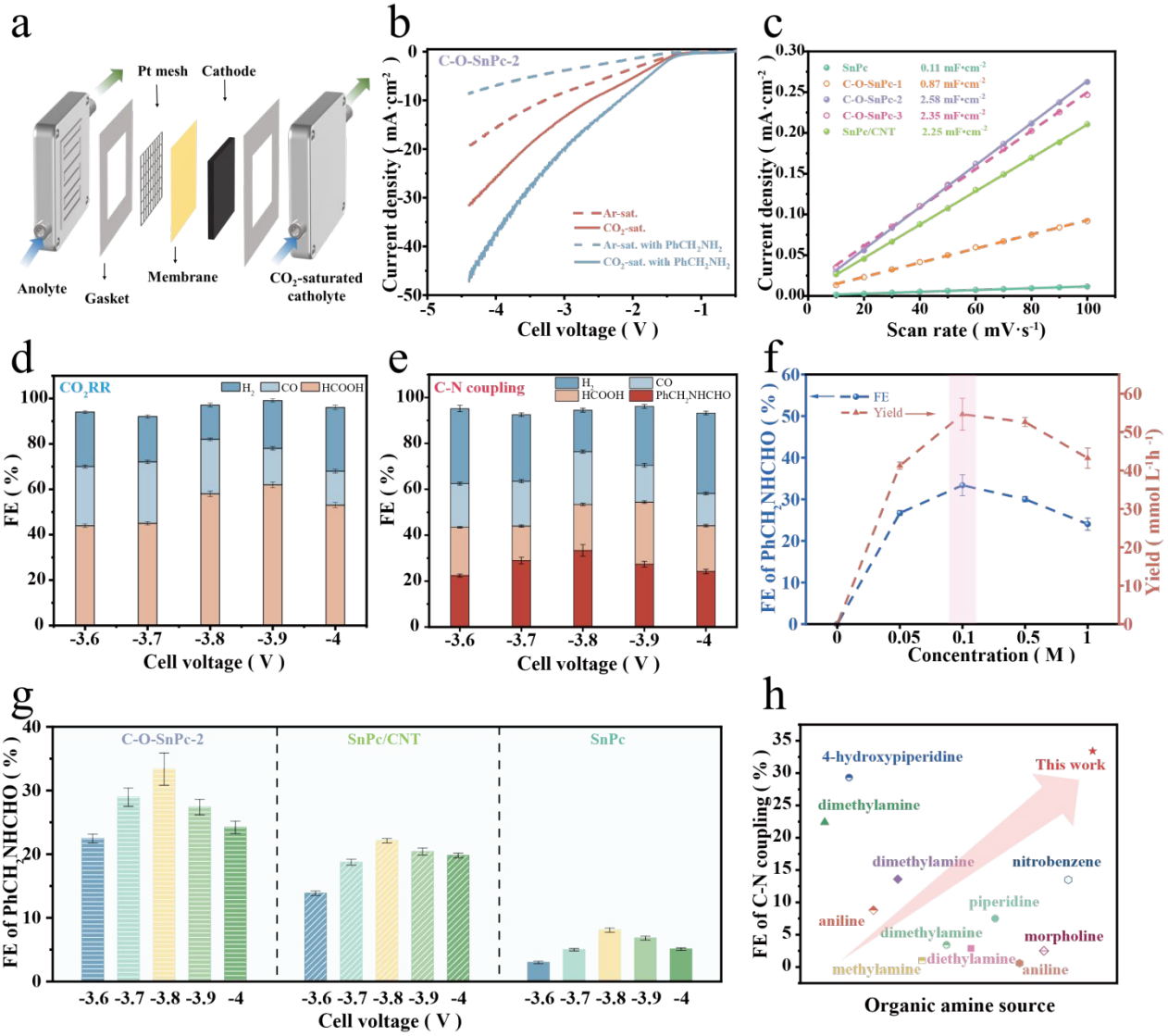

Fig. 1 (a) Schematic diagram of MEA cell. (b) LSV curves of C-O-SnPc-2 catalyst under four different conditions. (c) Calculated Cdl values of catalysts. Product distribution of (d) CO2RR and (e) C-N coupling under various potentials on C-O-SnPc-2. (f) FE and yield of C-N coupling product N-benzylformamide with different concentrations of benzylamine on C-O-SnPc-2. (g) FEs for N-benzylformamide of C-O-SnPc-2, SnPc/CNT, and SnPc under different applied cell voltage. (h) Comparison of other C-N coupling results using CO2 and amines as reactants.

infrared spectroscopy (FT-IR) spectra also confirmed this conclusion (Fig. S7), with C-O-SnPc-x and SnPc/CNT showing the signals of SnPc. X-ray diffraction (XRD) patterns (Fig. S8) revealed the structural evolution of the catalysts. C-O-SnPc-x samples and SnPc/CNT exhibited characteristic peaks of carbon nanotubes, confirming that the CNT framework remained intact after composite formation, consistent with TEM and HAADF-STEM observations. Notably, diffraction peaks corresponding to SnPc were detected in SnPc/CNT and C-O-SnPc-3, suggesting that aggregation tends to occur at high SnPc loadings or on unfunctionalized CNT surfaces. The introduction of hydroxyl groups could improve the dispersion of SnPc, but excessively high loading may still lead to partial aggregation.

Prior to the electrochemical C-N coupling reaction, the intrinsic activity of the catalyst was investigated. LSV curves under varying reactant conditions revealed the synergistic effects between reactants and the changes in the activity of catalysts (Fig. 1b and Fig. S9). In CO_2-saturated $KHCO_3$ containing 0.1 M benzylamine electrolyte, the current densities of all catalysts (SnPc, C-O-SnPc-x, SnPc/CNT) exceeded their responses in pure CO_2-saturated $KHCO_3$ (only CO_2RR) or Ar-saturated benzylamine electrolytes, indicating a novel synergistic reaction between CO_2 and benzylamine (C-N coupling) at the electrode surface. As shown in Fig. S10, the current density in C-N coupling at various potentials followed the order: C-O-SnPc-3 ≈ C-O-SnPc-2 > C-O-SnPc-1 > SnPc/CNT > SnPc. Specifically, C-O-SnPc-3 exhibited a slightly higher current density than C-O-SnPc-2, while both were significantly larger than the other catalysts. Inductively coupled plasma mass spectrometry (ICP-MS) and EDS mapping results (Table S1) showed that Sn loading increases from C-O-SnPc-1 to C-O-SnPc-3 (ICP: 2.8 → 3.9 → 4.5 wt%), yet the current density of C-O-SnPc-3 is only comparable to that of C-O-SnPc-2. Together with the lowest current density of pure SnPc (12.4 wt%), it confirmed that bridging-oxygen coordination and optimal dispersion, not merely higher Sn loading, enhance charge transfer in the C-N coupling reaction.

Subsequently, the electrochemically active surface area (ECSA) of these catalysts was investigated through cyclic voltammetry (CV) at different scan rates under open-circuit potential (OCP) (Fig. S11), yielding their double-layer capacitance (Cdl) values (Fig. 1c and Table S2). Pristine SnPc exhibited an extremely low ECSA (2.75 cm^{-2}), consistent with its poor conductivity and inherent tendency to aggregate, resulting in a limited number of exposed active sites. When SnPc was loaded on CNT-OH to form C-O-SnPc-1, its ECSA increased to 21.75 cm^{-2}. Furthermore, as the loading amount of SnPc increased, the ECSA exhibited a volcanic-type trend (21.75 → 64.5 → 58.75 cm^{-2}). This demonstrated that bridging oxygen prevented SnPc molecular aggregation acting as an effective anchoring site. When SnPc was loaded on CNT, its ECSA was 56.28 cm^{-2}, yielding the ECSA order: C-O-SnPc-2 > C-O-SnPc-3 > SnPc/CNT > C-O-SnPc-1 > SnPc. The observed variation in ECSA is closely linked to the electronic structure of the Sn active sites. To further discriminate between geometric and electronic contributions to the enhanced current density of C-O-SnPc catalysts, two complementary analyses were performed. First, the current densities in C-N coupling were normalized by the ECSA values to obtain the ECSA-normalized current density (j/ECSA). As shown in Fig. S12, j/ECSA for C-O-SnPc-2 was slightly higher than that for SnPc/CNT, suggesting that geometric area alone cannot account for the activity gap. (Pure SnPc exhibited an anomalously high j / ECSA due to its extremely low ECSA, but its absolute current density was negligible.) Then, CV curves in Ar-saturated 0.1 M $KHCO_3$ were used to probe the density of electrochemically accessible Sn^{4+} sites (Fig. S13).[38,39] A reduction peak corresponding to $Sn^{4+} \rightarrow Sn^{2+}$ was observed at approximately –0.13 to 0.13 V vs. RHE. The reduction peak current (i_p) followed the order: C-O-SnPc-2 > C-O-SnPc-3 > SnPc/CNT > C-O-SnPc-1 > SnPc. Notably, ICP-MS confirmed that C-O-SnPc-2 and SnPc/CNT have nearly identical total Sn loadings (3.9 wt% vs. 3.7 wt%), yet C-O-SnPc-2 exhibited a higher i_p, demonstrating that bridging-oxygen coordination significantly increases the fraction of accessible Sn^{4+} sites. Furthermore, the reduction peak potentials for C-O-SnPc-2 and C-O-SnPc-3 were slightly more negative than those for SnPc/CNT and C-O-SnPc-1. A more negative reduction potential reflected a higher thermodynamic stability of the Sn^{4+} state, meaning that the electron-deficient Sn^{4+} sites were more stable and required a larger overpotential to be reduced. It revealed that the superior activity of C-O-SnPc-2 originated from both a larger ECSA (geometric effect) and an enhanced intrinsic activity (electronic effect) induced by bridging-oxygen coordination.

To elucidate the underlying mechanism, X-ray photoelectron spectroscopy (XPS) was employed to analyse the chemical states of catalysts and calculate the relative proportions of different species. As shown in the Sn 3d XPS spectra (Fig. S14a, S15a and S16a), two distinct doublets were observed for all catalysts before electrolysis. The group at lower binding energy was assigned to Sn^{2+}, while the group at higher energy corresponded to Sn^{4+} (including surface-oxidized tin and oxygen-coordinated tin).[40] These results confirmed that the active sites initially present in all catalysts comprised a mixture of Sn^{2+} and Sn^{4+} species. Notably, the Sn^{4+} peaks in the C-O-SnPc-x catalysts showed a slight positive shift relative to those in SnPc/CNT, likely due to the electron-withdrawing effect of the bridging oxygen coordination to Sn centers. The Sn^{4+}/Sn^{2+} ratio followed the order: SnPc > C-O-SnPc-1 > SnPc/CNT ≈ C-O-SnPc-3 > C-O-SnPc-2 (Fig. S17a). In the O 1s XPS spectra (Fig. S14b, S15b and S16b), the peak at 530.4 eV was attributed to Sn-O bonding, with the remaining peaks corresponding to various carbon-oxygen compounds.[41] Pure SnPc was dominated by disordered Sn-O species (72.9%, Fig. S17b), indicating an oxide-rich surface. By contrast, all C-O-SnPc-x samples showed detectable C-O species signals and a markedly lower Sn-O content. These results demonstrated that the hydroxyl groups introduced on CNT effectively inhibited the deep oxidation of Sn active sites. These findings highlighted that both the introduction of bridging oxygen coordination and an appropriate SnPc loading are critical for enhancing the intrinsic activity of the catalysts.

View Article Online
DOI: 10.1039/D6GC01435F

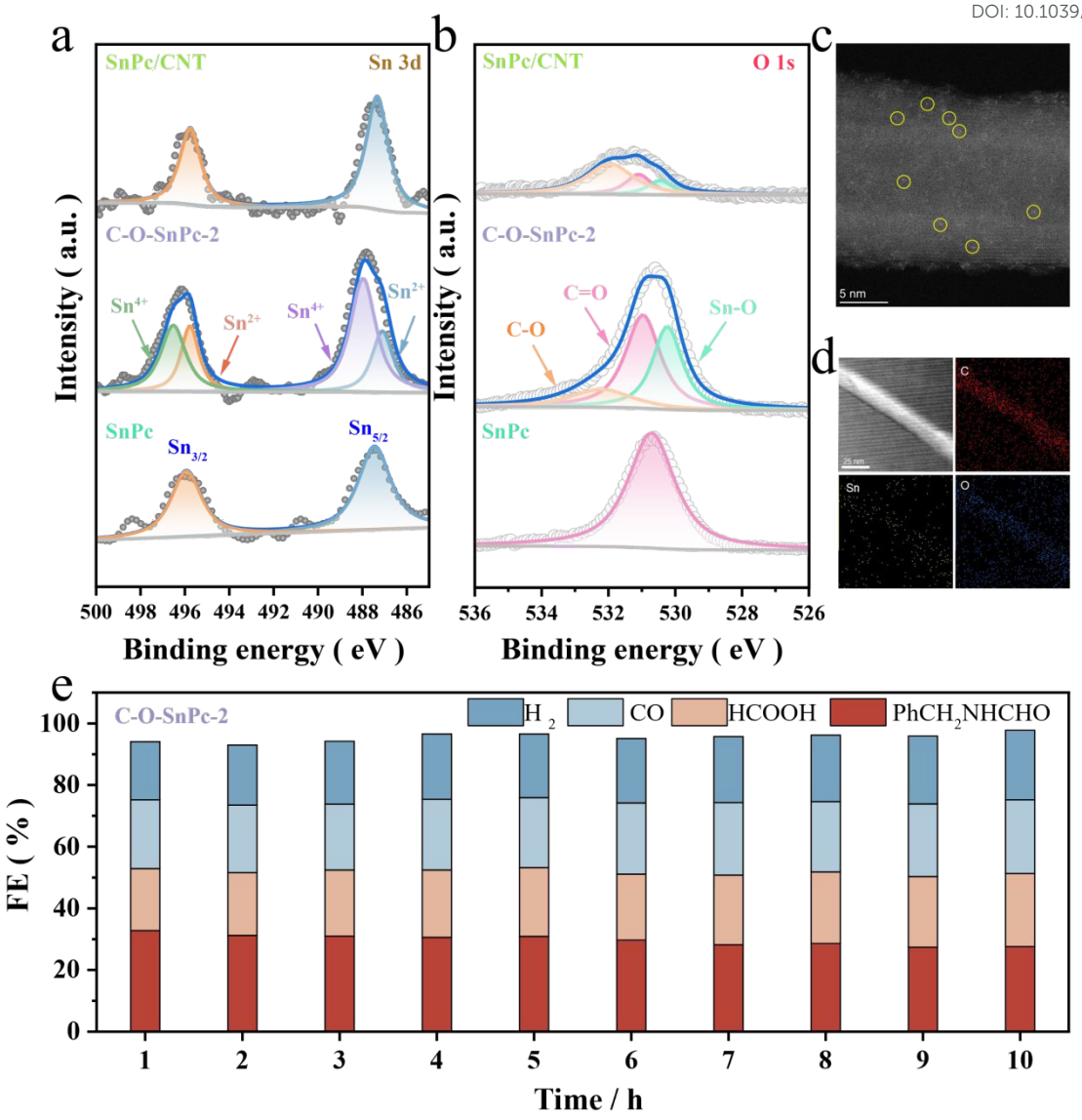

Fig. 2 (a) Sn 3d and (b) O 1s XPS spectra of SnPc/CNT, C-O-SnPc-2, and SnPc catalysts after electrolysis. (c) HAADF-STEM image of C-O-SnPc-2 catalyst before electrolysis. (d) EDS mapping of C-O-SnPc-2 catalyst after electrolysis. (e) Product FEs in the long-term stability of CO_2 and benzylamine C-N coupling on the C-O-SnPc-2 catalyst at a cell voltage of –3.8 V in MEA cell.

The CO_2RR performance of C-O-SnPc-2 was evaluated firstly as shown in Fig. 1d, with the gaseous and liquid products consisting of H_2, formic acid, and CO. When comparing the evolution of product distribution in C-N coupling (Fig. 1e) and CO_2RR on C-O-SnPc-2, the target product N-benzylformamide was formed over the potential range of –3.6 V to –4.0 V in the presence of benzylamine. At the same potential, the FEs for formate and CO in the C-N coupling process were lower than CO_2RR, while the FE for H_2 was higher than CO_2RR. This indicated that the reaction pathway involving benzylamine competed with the pathways for formate and CO formation. Besides, the effect of benzylamine concentration on the selectivity of the C-N coupling products was then investigated. As shown in Fig. 1f, the FE of N-benzylformamide followed a volcanic trend with increasing benzylamine concentration, reaching a maximum at 0.1 M benzylamine. In the low concentration range (0 – 0.1 M), the gradual increase in FE can be primarily ascribed to kinetic acceleration. As a nucleophile, increasing benzylamine concentration directly enhanced the collision frequency between benzylamine molecules and the key intermediate in CO_2 reduction at the electrode interface. At higher concentrations, however, strong adsorption or multilayer coverage of benzylamine molecules may occur, which can block active sites and hinder mass transfer process, thereby leading to a decline in FE.

Fig. 1g and Fig. S18 showed the FEs and corresponding yields for the C-N coupling product N-benzylformamide on C-O-SnPc-2, SnPc/CNT, and SnPc and detailed product distributions for SnPc, C-O-SnPc-x and SnPc/CNT were shown in Fig. 1e and Fig. S19. For different catalysts, FEs exhibited a volcano-shaped curve as the cell voltage increased. This indicated the existence of an optimal potential window. Kinetic driving force was insufficient at excessively

low potentials; while excessively negative potentials intensified competitive hydrogen evolution reaction (HER). Among the catalysts, C-O-SnPc-2 exhibited optimal performance, achieving 33.4% of FE at –3.8 V cell voltage with the yield of 53 mmol·L^{-1}·h^{-1}. It consistently outperformed SnPc/CNT and pure SnPc across all tested potentials. Notably, its peak FE was about 1.5 and 4 times higher than those of SnPc/CNT (22.1%, 37.7 mmol·L^{-1}·h^{-1}) and pure SnPc (8.1%, 8.4 mmol·L^{-1}·h^{-1}), respectively, providing strong validation for the bridging oxygen axial coordination strategy. Notably, it is found that C-O-SnPc-2 catalyst showed outstanding C-N coupling performance comparing with other catalysts towards C-N coupling using CO_2 and amines as reactants (Fig. 1h and Table S3).

Subsequently, the performance of C-O-SnPc-x was compared. At potentials ranging from –3.6 V to –3.9 V, the performance order was C-O-SnPc-2 > C-O-SnPc-3 > C-O-SnPc-1. At –4.0 V, the FE of C-O-SnPc-3 was lower than C-O-SnPc-1, suggesting that the excessive SnPc loading in C-O-SnPc-3 may reduce selectivity due to partial aggregation. Interestingly, at relatively mild potentials (–3.6 to –3.8 V), SnPc/CNT exhibited higher FEs than C-O-SnPc-1, likely due to its superior conductivity and initial active site density. However, at more negative potentials (–3.9 to –4.0 V), C-O-SnPc-1 showed superior selectivity. This demonstrated the advantage of bridging oxygen coordination in resisting reduction and maintaining high selectivity under harsh conditions.

To uncover the structural origin of this superior catalytic performance, post-electrolysis XPS characterizations were conducted to analyse the chemical states of Sn and O species on the catalyst surfaces. Fig. 2a, 2b, and Fig. S20, S21 showed the Sn 3d and O 1s XPS spectra for SnPc, C-O-SnPc-x, and SnPc/CNT after electrolysis. C-O-SnPc-2 exhibited the highest Sn^{4+}/Sn^{2+} ratio (Fig. S22a), while the ratios for SnPc and SnPc/CNT decreased to 0. It revealed that the Sn^{4+} species in post-electrolysis C-O-SnPc-2 originated from the bridging oxygen coordination to Sn. Oxides attributed to Sn^{4+} on the pre-reaction catalyst surface were reduced during electrolysis, leaving O-anchored Sn^{4+} sites. This observation was consistent with the mentioned C-N coupling performance, where C-O-SnPc-2 retained more anchored Sn^{4+} sites after reaction, followed by C-O-SnPc-3 and C-O-SnPc-1. Additionally, in Fig. S22b, although the Sn-O species proportions in SnPc and SnPc/CNT were higher than that in C-O-SnPc-2, their signal intensities were significantly lower than the latter, further indicating the disappearance of the oxide species. These results confirmed the importance of bridging oxygen coordination for constructing highly efficient C-N coupling active sites.

In the HAADF-STEM image in Fig. 2c, C-O-SnPc-2 showed tube structure and uniform Sn single atom distribution. After 10-hour constant-potential electrolytic stability test conducted at a potential of –3.8 V, the TEM and scanning electron microscopy (SEM) images in Fig. 2d and Fig. S23 showed the catalyst retained complete structure without obvious collapse and SnPc agglomeration. During the initial stage, the N-benzylformamide FE in Fig. 2e reached 32.8%, and after 10 hours, the FE was still maintained at 27.6%. As shown in Fig. S24, the current density remained relatively stable throughout the test without significant decline. The results demonstrated that C-O-SnPc-2 exhibited excellent long-term stability.

Intermediates and reaction pathway

To investigate the reaction pathway of electrocatalytic C-N coupling, liquid product detection was first conducted under varied reaction conditions via ^{1}H NMR spectra. As shown in Fig. S25a, when only CO_2 was used under applied potential, only formic acid was detected in the liquid product. When only benzylamine ($PhCH_2NH_2$) was used as the reactant, only benzylamine was detected in the liquid product. No new products were detected in the mixed reactants of CO_2 and benzylamine without current (Fig. S25b), ruling out the possibility of thermodynamically spontaneous reactions. Under applied potential, N-benzylformamide and formate were detected, indicating the reaction is electrochemically driven (Fig. S25c). Crucially, as previously noted, the C-N coupling pathway may compete with the conversion of CO_2 to formate pathway. Therefore, formic acid was directly substituted for CO_2 in the electrochemical reaction, yet no N-benzylformamide was formed (Fig. S25d). It indicated that the intermediate involved in C-N coupling was likely an active adsorbed intermediate reduced at the electrode surface, rather than the formic acid molecule. This intermediate was nucleophilically attacked by the co-adsorbed benzylamine, confirming that the reaction followed a tandem electrochemical-chemical process. Though it was found that C-N coupling proceeded via a tandem mechanism involving key intermediates, the coupling mechanism of CO_2 and benzylamine remains unclear. To further capture reaction intermediates in real time and elucidate the C-N coupling mechanism, *in situ* electrochemical spectroscopy and mass spectrometry characterization of the catalysts were performed.

In Fig. 3a and d, *in situ* Fourier transform infrared spectroscopy (FT-IR) revealed no distinct characteristic peaks on the C-O-SnPc-2 surface at OCP. However, when a potential was applied, characteristic peaks attributed to *COOH (1660 cm^{-1}), *C-O species (1178 cm^{-1}), and C-N bond (1357 cm^{-1}) could be observed.[18, 42] FT-IR spectra under varied conditions (in Fig. S26) confirmed that the potential-induced C-N peak at 1357 cm^{-1} is not from free benzylamine nor from mere benzylamine adsorption, but originates from CO_2-dependent surface intermediates. The three peaks were also observed on SnPc/CNT (Fig. 3b and e), but the intensity of the C-N bond peak was significantly reduced (Fig. 3i), consistent with its lower catalytic efficiency. On SnPc surface, only *COOH and $*CO_B$ was detected, indicating the conversion of CO_2 to *CO or HCOOH (Fig. 3c and f). Furthermore, compared to C-O-SnPc-2, the peak intensities of the *COOH intermediate and C-N bond on the C-O-SnPc-1 surface were lower, consistent with its reduced FEs for C1 products and C-N coupling products (Fig. 3g). Meanwhile, C-O-SnPc-3 exhibited lower FE for coupling product than C-O-SnPc-2 but higher FEs for C1 products, a finding consistent with the changes in peak intensities in the *in situ* FT-IR spectra (Fig. 3h). The integrated intensities of the C-N bond (1357 cm^{-1}) and *COOH (1660 cm^{-1}) peaks from *in situ* FT-IR spectra represented the relative surface concentrations of the corresponding intermediates, which were substantially higher on C-O-SnPc-2 than on SnPc/CNT and SnPc, qualitatively consistent with the enhanced catalytic activity. The spectroscopic tracking confirmed that the bridging-oxygen-coordinated Sn sites in C-O-SnPc-2 effectively stabilized the key *COOH intermediate and facilitated its

subsequent coupling with benzylamine.

View Article Online
DOI: 10.1039/D6GC01435F

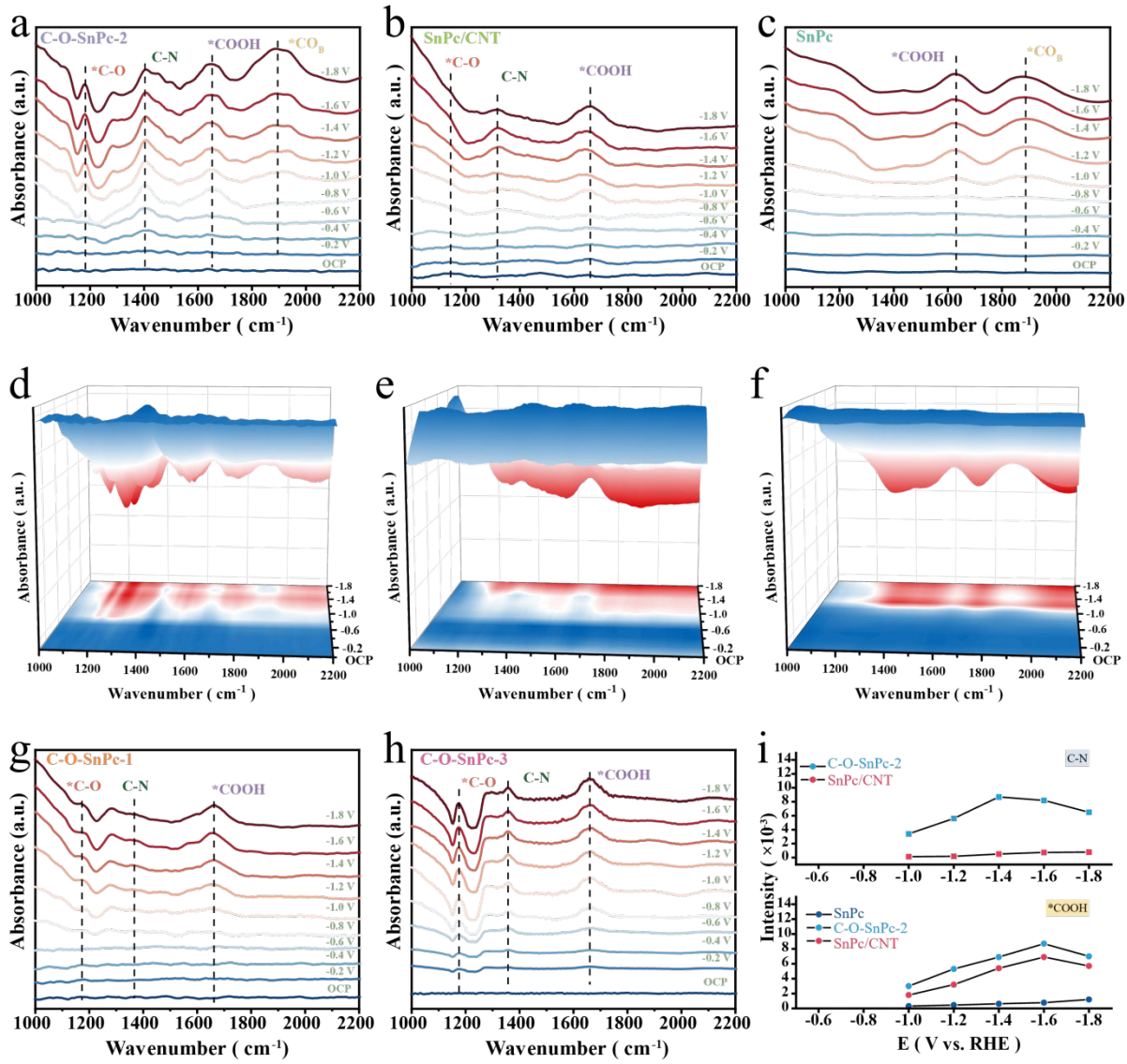

Fig. 3 *In situ* FT-IR detection for intermediates during C-N coupling on (a) C-O-SnPc-2, (b) SnPc/CNT, (c) SnPc and (d–f) corresponding three-dimensional *in situ* FT-IR spectra. *In situ* FT-IR spectra on (g) C-O-SnPc-1 and (h) C-O-SnPc-3. (i) Detected intermediate intensity of the C-N bond (top part), and *COOH (bottom part) for C-O-SnPc-2, SnPc/CNT, and SnPc. The data in (i) are semi-quantitative and reflect surface-bound intermediates.

In situ electrochemical Raman spectroscopy also provided direct spectroscopic evidence for the proposed underlying reaction pathway. As shown in Fig. 4a for C-O-SnPc-2, upon applying increasingly negative potentials, a well-defined peak emerged at 1000 cm^{-1}, which was attributed to the *COOH intermediate. Meanwhile, a peak corresponding to the carbonate group (CO_3^{2-}) was observed at 1030 cm^{-1}, and a peak at 1200 cm^{-1} was assigned to C-N bond.[19] The observations revealed that the C-N coupling proceeded via a *COOH-mediated pathway on the catalyst surface.

Furthermore, online differential electrochemical mass spectrometry (DEMS) was employed to detect the mass-to-charge (m/z) ratios of molecular intermediate species in the electrochemical C-N coupling of CO_2 and benzylamine (Fig. 4b). During three continuous electrochemical cycles, signals were detected at m/z = 2, 28, 29, 45, and 60, suggesting the presence of H_2, CO, HCOOH, and the C-N coupling intermediate *NHCOOH, respectively. These results indicated that during C-N coupling, CO_2 was reduced to the *COOH intermediate. A portion of *COOH proceeded along the CO_2 reduction reaction pathway to form formic acid and CO, while another portion underwent nucleophilically attack by amine to initiate C-N coupling. On the basis of *in situ* characterization findings, the reaction pathway could be inferred as follows: CO_2 was activated to form *COOH; then *COOH was nucleophilically attacked by benzylamine to generate *PhCH$_2$NHCOOH; then it was followed by hydrogenation and dehydration steps to yield the target product N-benzylformamide: CO_2 + $PhCH_2NH_2$ → *COOH + *$PhCH_2NH$ → *$PhCH_2NHCOOH$ → *$PhCH_2NHCH_2O_2$ → *$PhCH_2NHCHO$ (Fig. 4c).

View Article Online
DOI: 10.1039/D6GC01435F

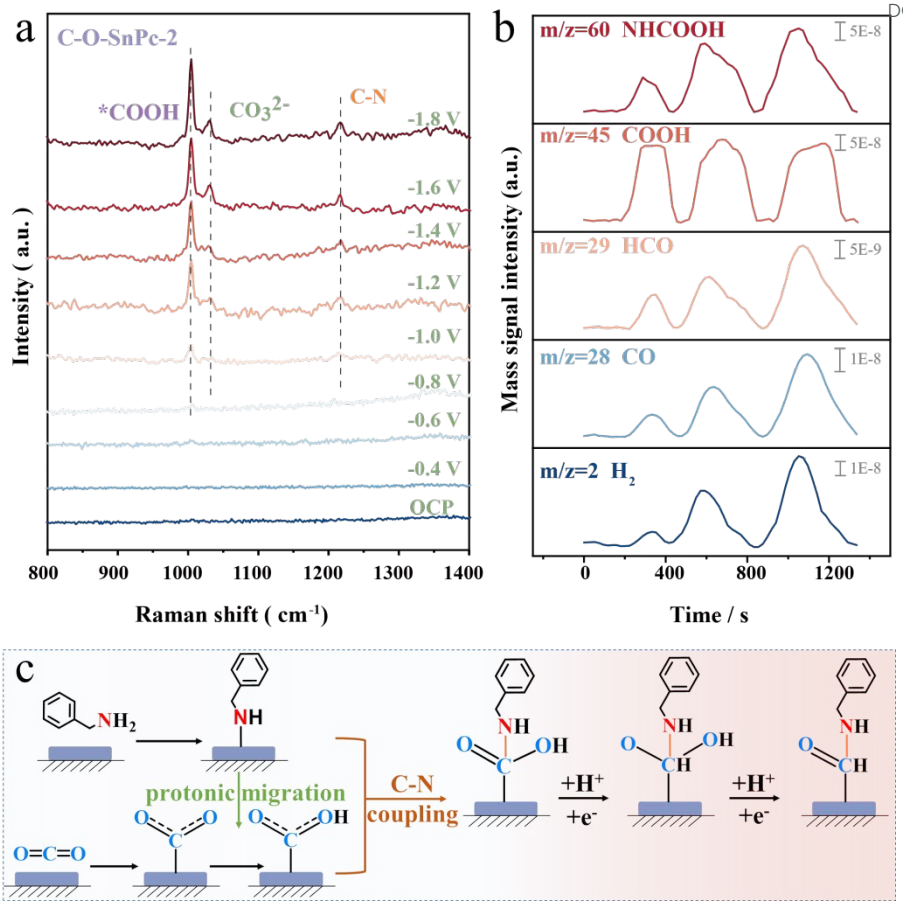

Fig. 4 (a) *In situ* Raman spectra during C-N coupling on C-O-SnPc-2. (b) Online DEMS spectra of C-O-SnPc-2 during C-N coupling. (c) Schematic diagram of C-N coupling achieved by using CO_2 and benzylamine.

DFT calculations and catalytic mechanism

To further clarify the mechanism by which hydroxyl-modified bridging oxygen coordination enhanced C-N coupling performance, density functional theory (DFT) calculations were performed. The adsorption energies of CO_2 and benzylamine molecules co-adsorbed on C-O-SnPc-2 and SnPc/CNT surfaces were calculated (Fig. 5a and b). The adsorption energy of C-O-SnPc-2 was –1.17 eV, significantly lower than SnPc/CNT (–0.58 eV). It indicated that C-O-SnPc-2, with bridging oxygen coordination, could more effectively stabilize both reactants near the active site, providing the basis for subsequent surface reactions. Furthermore, differential charge density analysis of C-O-SnPc-2 revealed that the electron transfer number was 1.933, compared to 1.566 e for SnPc/CNT, confirming that oxygen coordination significantly enhanced electron interactions between the metal and support. The bent geometry of SnPc plays a critical role in the observed catalytic enhancement. The out-of-plane Sn center became sterically accessible to both CO_2 and benzylamine, while the highly electronegative bridging oxygen withdrew electrons from the Sn center, decreasing its electron density and making it more electron-deficient (cyan region in Fig. 5c). Simultaneously, the electron-deficient Sn center withdrew electrons from the electron cloud of the benzylamine amino group, thereby weakening the N-H bond. It promoted proton dissociation and facilitated the activation of CO_2 to the *COOH intermediate through a proton transfer process. The oxygen atom in *COOH, possessing higher electron density, was attracted toward the Sn center, enhancing the surface stability of *COOH. Concurrently, this effect indirectly reduced the electron density on the carbon atom of *COOH, boosting its electrophilicity and facilitating the subsequent nucleophilic attack by benzylamine to form the C-N bond. In SnPc/CNT, the Sn center was primarily influenced by the phthalocyanine ring, exhibiting relatively higher electron density and mainly displaying Sn^{2+} characteristics (Fig. 5d).

The free energies for key steps in the process from the generation of the *COOH intermediate to the final formation of *$PhCH_2NHCHO$ were calculated after CO_2 and benzylamine were co-adsorbed on C-O-SnPc-2 and SnPc/CNT surfaces (Fig. 5e), along with the structurally optimized models for the corresponding steps (Fig. 5f). The co-adsorption of reactants on both C-O-SnPc-2 and SnPc/CNT were spontaneous, whereas it was more favourable on C-O-SnPc-2. Subsequently, during the formation of *COOH, C-O-SnPc-2 reduced the reaction energy barrier (Fig. S27), confirming the stabilizing effect of the Sn center on the *COOH after bridging oxygen coordination. The following C-N coupling to form *$PhCH_2NHCOOH$ occurred as an exothermic and spontaneous process on both C-O-SnPc-2 and SnPc/CNT, while C-O-SnPc-2 provided more thermodynamically favourable conditions (ΔG = −0.21 eV).

View Article Online
DOI: 10.1039/D6GC01435F

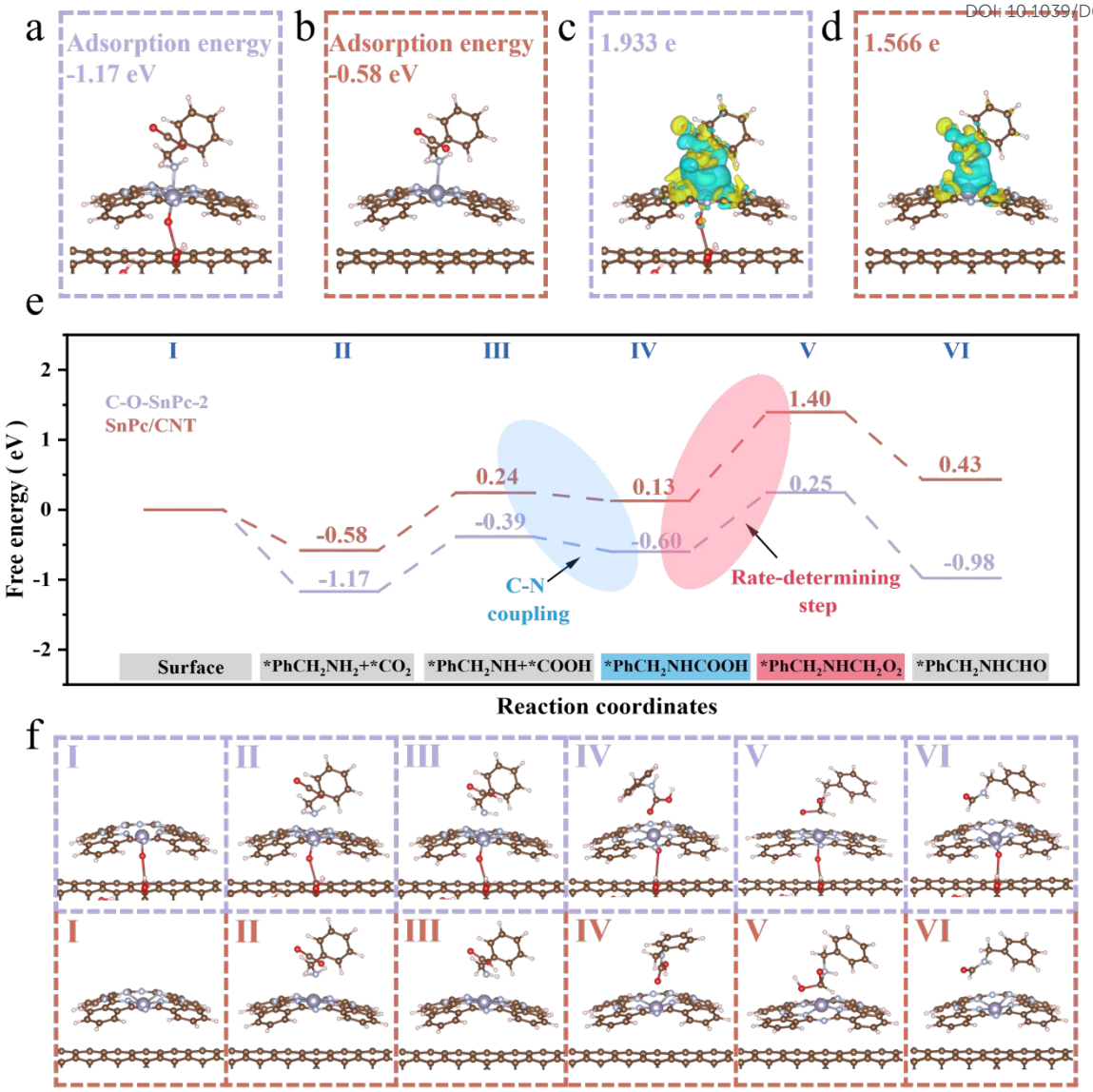

Fig. 5 The co-adsorption energy for CO_2 and benzylamine on (a) C-O-SnPc-2 and (b) SnPc/CNT. Differential charge density of (c) C-O-SnPc-2 and (d) SnPc/CNT. (e) Free energy for the binding of intermediates along the reaction coordinates on C-O-SnPc-2 and SnPc/CNT. (f) Structural optimization modeling for the C-N coupling pathway on C-O-SnPc-2 (purple boxes) and SnPc/CNT (red boxes).

Then the hydrogenation step acted as the RDS of the C-N coupling process. The energy barrier for RDS was significantly lower on C-O-SnPc-2 (ΔG = 0.85 eV) compared to SnPc/CNT (ΔG = 1.27 eV). Furthermore, for the critical dehydration step, C-O-SnPc-2 showed a highly exothermic and spontaneous character (ΔG = –1.23 eV), offering a strong thermodynamic driving force for the reaction. In contrast, the driving force was much weaker on SnPc/CNT (ΔG = –0.97 eV). Theoretical calculations revealed that axial Sn-O coordination enhanced reactant adsorption capacity, significantly lowered the RDS energy barrier by selectively stabilizing key reaction intermediates (*COOH and *$PhCH_2NHCOOH$), and simultaneously provided a stronger thermodynamic driving force. This enabled the C-N coupling process on C-O-SnPc-2 to be more favourable both kinetically and thermodynamically.

In addition, different substrate tests (as shown in Fig. S28 and S29) on C-O-SnPc-2 showed that dimethylamine gave N,N-dimethylformamide ($HCON(CH_3)_2$) with FE ~ 38% (higher than benzylamine 33.4%), while aniline formed only trace formanilide (FE < 10%). The three amines are arranged in descending order of nucleophilicity: dimethylamine > benzylamine > aniline. The bridging-oxygen coordinated Sn^{4+} center overcame the lower nucleophilicity of benzylamine, need for N-H activation, and larger steric hindrance by enhancing *COOH electrophilicity, polarizing the N-H bond, and providing a non-bulky adsorption architecture at optimal SnPc loading (3.9 wt% Sn). It may guide catalyst design for other demanding amines with different nucleophilicity.

Conclusions

In summary, we report for the first time the electrocatalytic synthesis of N-benzylformamide via the C-N coupling of CO_2 and benzylamine on C-O-SnPc-2 using a green, mild electrochemical approach. The C-O-SnPc-2 catalyst, synthesized by bridging oxygen coordination anchoring the Sn center, achieved a peak selectivity of 33.4% for N-benzylformamide synthesis at the yield of 53 $mmol \cdot L^{-1} \cdot h^{-1}$. *In situ* FT-IR, Raman, and online DEMS confirmed the C-N coupling reaction pathway. Theoretical calculations revealed that bridging oxygen coordination reduced the electron density at the Sn center, making it more electron-deficient. It increased adsorption capacity for reactants on C-O-SnPc-2, promoting their initial activation and enrichment. Then the electron-withdrawing effect enhanced the stabilization of key intermediate, increasing the electrophilicity on the carbon atom and favouring nucleophilically attack by benzylamine. Free energy analysis of the reaction pathway indicated that on the C-O-SnPc-2 surface, the conversion steps from reactant adsorption to the final product $PhCH_2NHCHO$ were more thermodynamically favourable. Notably, the energy barriers for both the C-N coupling step and the RDS were significantly reduced. This work provides a novel green strategy for the high-value utilization of CO_2 and organic amines, offering an alternative pathway design for CO_2 resource utilization that is distinct from traditional carbon-containing products.

Author contributions

Xiaoqian Gao: Conceptualization, Investigation, Writing – original draft. Chufan Li: Validation, Formal analysis. Jingyan Liu: Formal analysis, Data curation. Shaohan Xu: Writing – review and editing. Kuang Chen: Investigation. Guohua Zhao: Project administration, Conceptualization, Writing – review and editing, Supervision.

Conflicts of interest

There are no conflicts to declare.

Data availability

The data supporting this article have been included as part of the ESI. The supplementary information includes detailed electrochemical measurements, *in situ* experiments, product analysis and characterization. It also provides supplementary figures and tables.

Acknowledgements

This work was financially supported by the National Key R&D Program of China (grant No. 2024YFA1211003), the National Natural Science Foundation of China (NSFC, grant Nos. 22476153 and 21537003), and the Tongji University Medicine-X Interdisciplinary Research Initiative (grant No. 2025-0313-ZD-02).

References

1. M. L. Sun, H. Y. Wang, Y. Feng, J. T. Ren, L. Wang and Z. Y. Yuan, *Chem. Soc. Rev.*, 2024, 53, 11908-11966.
2. P. Y. Shi, Y. Yan, S. Y. Yang, J. J. Hao, M. Wang and T. B. Lu, *Chem. Sci.*, 2025, 16, 11711-11739.
3. W. Zhou, X. Li, X. Tu, H. Zhao, Q. Li, Z. Liu, D. Sun, X. Liu, M. Huang, J. Zhu and H. Jiang, *Nano Research*, 2025, 18.
4. Z. Tao, C. L. Rooney, Y. Liang and H. Wang, *J. Am. Chem. Soc.*, 2021, 143, 19630-19642.
5. J. Zheng, S. Xu, L. Sun, X. Pan, Q. Xie, L. Li, J. Cai and G. Zhao, *Adv. Energy Mater.*, 2024, 14.
6. A. Kumar, P. Sharma, N. Sharma, Y. Kumar and D. Mahajan, *RSC Adv.*, 2021, 11, 25777-25787.
7. L. Lombardo, Y. Ko, K. Zhao, H. Yang and A. Zuttel, *Angew. Chem. Int. Ed.*, 2021, 60, 9580-9589.
8. L. Zhang, Z. Han, X. Zhao, Z. Wang and K. Ding, *Angew. Chem. Int. Ed.*, 2015, 54, 6186-6189.
9. X. Dai, T. Li, B. Wang, C. Kreyenschulte, S. Bartling, S. Liu, D. He, H. Yuan, A. Bruckner, F. Shi, J. Rabeah and X. Cui, *Angew. Chem. Int. Ed.*, 2023, 62, e202217380.
10. D. Zhao, Z. Chen, W. Yang, S. Liu, X. Zhang, Y. Yu, W. C. Cheong, L. Zheng, F. Ren, G. Ying, X. Cao, D. Wang, Q. Peng, G. Wang and C. Chen, *J. Am. Chem. Soc.*, 2019, 141, 4086-4093.
11. Y. He, D. D. Ma, K. Ma, X. Li, L. Han, X. T. Wu and Q. L. Zhu, *Nat. Commun.*, 2025, 16, 3564.
12. C. Zhao, Y. Jin, J. Yuan, Q. Hou, H. Li, X. Yan, H. Ou and G. Yang, *J. Am. Chem. Soc.*, 2025, 147, 8871-8880.
13. M. Xu, M. Wang, H. Wang, P. Yuan, Q. Han and G. Zheng, *Adv. Mater.*, 2025, 2507144.
14. J. Zheng, S. Xu, J. Sun, J. Zhang, L. Sun, X. Pan, L. Li and G. Zhao, *Appl. Catal. B*, 338 (2023) 123056.
15. S. Kuang, T. Xiao, H. Chi, J. Liu, C. Mu, H. Liu, S. Wang, Y. Yu, T. J. Meyer, S. Zhang and X. Ma, *Angew. Chem. Int. Ed.*, 2024, 63, e202316772.
16. X. Wei, S. Q. Liu, H. Liu, Y. Ding, P. X. Lei, S. Wu, L. Song, X. Z. Fu and J. L. Luo, *J. Am. Chem. Soc.*, 2025, 147, 6049-6057.
17. Y. Zhang, Z. Li, C. Qiang, K. Chen, Y. Guo and K. Chu, *ACS Nano*, 2024, 18, 25316-25324.
18. P. Bai, J. Chen, Y. Zhao and Y. Li, *Nano Energy*, 2025, 135, 110673.
19. Y. Fan, T. Liu, Y. Yan, Z. Xia, Y. Lu, Y. Pan, R. Wang, D. Xie, Z. Zhu, T. T. T. Nga, C.-L. Dong, Y. Jing, Y. Li, S. Wang and Y. Zou, *Chem*, 2024, 10, 2437-2449.
20. J. Zheng, S. Xu, L. Sun, X. Pan, Q. Xie and G. Zhao, *Energy Environ. Sci.*, 2025, 18, 3614-3622.
21. C. L. Rooney, Y. Wu, Z. Tao and H. Wang, *J. Am. Chem. Soc.*, 2021, 143, 19983-19991.
22. L. Li, Y. Zhou, C. Wan, X. Li, P. Qiao, S. Xi, Y. Fang, X. Fu, J. Zhu, S. Wang, X. Wang, C. Xu, Z. Zhuang, M. Zuo, M. Fan, Z. Jiang, W. Zhang, X. Feng, Y. Sun, J. Yang and Y. Xie, *Joule*, 2025, 9, 101926.
23. X. Ma, X. Song, X. Tan, L. Zhang, S. Jia, L. Wu, R. Wang, W. Li, C. Zheng, L. Jing, X. Kang, Q. Zhu, X. Sun and B. Han, *J. Am. Chem. Soc.*, 2025, 147, 27377-27389.
24. T. Wang, J. Chen, X. Ren, J. Zhang, J. Ding, Y. Liu, K. H. Lim, J. Wang, X. Li, H. Yang, Y. Huang, S. Kawi and B. Liu, *Angew. Chem. Int. Ed.*, 2023, 62, e202211174.

View Article Online
DOI: 10.1039/D6GC01435F

25. W. Liu, H. Li, P. Ou, J. Mao, L. Han, J. Song, J. Luo and H. L. Xin, *Nano Res*., 2023, 16, 8729-8736.
26. Y. Deng, J. Zhao, S. Wang, R. Chen, J. Ding, H. J. Tsai, W. J. Zeng, S. F. Hung, W. Xu, J. Wang, F. Jaouen, X. Li, Y. Huang and B. Liu, *J. Am. Chem. Soc.*, 2023, 145, 7242-7251.
27. X. Zhang, Z. Wu, X. Zhang, L. Li, Y. Li, H. Xu, X. Li, X. Yu, Z. Zhang, Y. Liang and H. Wang, *Nat. Commun.*, 2017, 8, 14675.
28. Z. S. Huang, Y. F. Wang, M. Y. Qi, M. Conte, Z. R. Tang and Y. J. Xu, *Angew. Chem. Int. Ed.*, 2024, 63, e202412707.
29. Y. Wang, X. Zhu, Q. An, X. Zhang, X. Wei, C. Chen, H. Li, D. Chen, Y. Zhou, Q. Liu, H. Shao and S. Wang, *Angew. Chem. Int. Ed.*, 2024, 63, e202410938.
30. G. Kresse and J. Hafner, *Phys. Rev. B Condens. Matter*, 1993, 48, 13115-13118.
31. G. Kresse and J. Hafner, *Phys. Rev. B Condens. Matter*, 1994, 49, 14251-14269.
32. G. Kresse and J. Furthmüller, *Comput. Mater. Sci.*, 1996, 6, 15-50.
33. P. N. Day, Z. Wang and R. Pachter, *J. Mol. Struct. THEOCHEM*, 1998, 455(1): 33-50.
34. G. Kresse and D. Joubert, *Phys. Rev. B*, 1999, 59, 1758-1775.
35. H. J. Monkhorst and J. D. Pack, *Phys. Rev. B*, 1976, 13, 5188-5192.
36. J. P. Perdew, K. Burke and M. Ernzerhof, *Phys. Rev. Lett.*, 1996, 77, 3865-3868.
37. X. Y. Wu, J. F. Lu, S. Zou, J. Zhao, S. L. Hou, Z. H. Zhu, H. Xu, S. J. Liu and H. R. Wen, *Adv. Funct. Mater.*, 2025, 35.
38. P. Li, Y. Yao, W. Zhong, W. Li, Q. Zhu, X. Wang and J. Jiang, *Angew. Chem. Int. Ed.*, 2025, 64, e202502118.
39. H. Liu, Y. Jin, A. Fauzi, Z. Liang, Z. Shen, X. Zhang, Y. Yu, W. Wang, L. Pan and S. Zhang, *Appl. Catal. B*, 388, 126559.
40. H. Liu, B. Li, Z. Liu, Z. Liang, H. Chuai, H. Wang, S. N. Lou, Y. Su, S. Zhang and X. Ma, *ACS Catal.*, 2023, 13, 5033-5042.
41. M. Pisarek, M. Krawczyk, M. Holdynski and W. Lisowski, *ACS Omega*, 2020, 5, 8647-8658.
42. H. Shi, H. Wang, Y. Zhou, J. Li, P. Zhai, X. Li, G. G. Gurzadyan, J. Hou, H. Yang and X. Guo, *Angew. Chem. Int. Ed.*, 2022, 61, e202208904.

View Article Online
DOI: 10.1039/D6GC01435F

The data supporting this article have been included as part of the ESI. The supplementary information includes detailed electrochemical measurements, *in situ* experiments, product analysis and characterization. It also provides supplementary figures and tables.